Chapter 6

Single Channel Laminar Flat Flame Simulations

6.1 Rational and Objectives

In chapter 5, full 2-D reacting flow simulation of the flat flame burner was reported. A second order fit was found to be appropriate to describe the flame dynamics predicted by the CFD model. However, the phase relationship between the unsteady heat release rate (q') and the incoming fluid stream velocity fluctuation (u') was not correctly predicted. Also, the low frequency resonance phenomenon was not captured. The objective of the second part of laminar forced response studies is to propose a CFD model that is able to correctly predict both magnitude and phase relationships between q' and u'. Several changes have been made to the original full 2-D CFD model and the new model is described in this section.

6.2 Computational Model

6.2.1 Computational Geometry and Grid Generation

The most important issue that was identified to cause a failure in the prediction of both magnitude and phase of the FRF, was the inability of the model to capture the flame shape. Reaction rate iso-contours are the measure for determining flame shape. In the full 2-D simulation, due to the large grid size requirement, the flame shape was not accurately captured. To reduce overall grid size while keeping the grid very fine downstream of the honeycomb exit, a 'single-channel approach' has been chosen for further studies of the flat flame dynamics. This approach is based on the assumption that the flat flame is nearly one-dimensional everywhere except at the edges (near the quartz chimney wall). Therefore, a computational geometry that includes one channel of the honeycomb and the corresponding upstream and downstream regions has been considered for the study. The computational domain is shown in Figure 6.1. The computational inlet is located $1\,cm$ upstream of the honeycomb inlet. The honeycomb is represented by two parallel fluid paths, each path being equal to half the width of the actual 2-D honeycomb fluid channel. A single honeycomb solid, with properties of Cordierite, is located at the center of geometry. The downstream length (corresponding to the height of the quartz chimney) is $14.62\,cm$. The flame stabilizes on top of the honeycomb solid (flame shown with wrinkled curves on the figure).

The computational grid generated (see Figure 6.2) is similar to the grid in the full 2-D simulations. Upstream of the honeycomb (inlet section), the grid first is quadrilateral structured (quad) and then changes to triangular unstructured (tri) just upstream of the honeycomb. This change is necessary to increase the grid density inside the honeycomb. The grid inside the honeycomb is made up of quad cells and it is body fitted to capture the velocity/thermal boundary layers. Downstream of the honeycomb (flame region) the grid comprises of triangular cells and the grid is the densest in this region. Multiple grid adaptations were carried out during the steady state calculations. Finally, the flame region grid density was decided

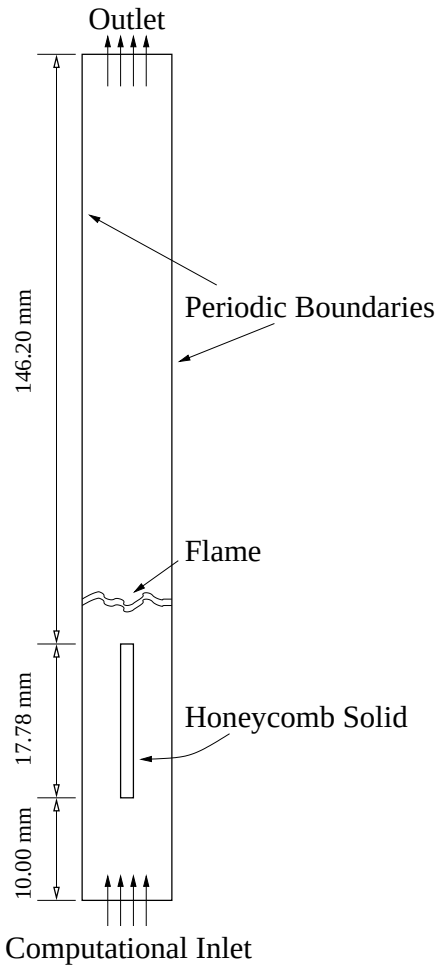

Figure 6.1: Single channel flat flame burner geometry

after the reaction rate iso-contours were found to be parallel with each other and perpendicular to the velocity vectors. Downstream of the flame region, a transition to coarse tri grid was introduced. Further downstream (outlet section) quad grid was generated to reduce the overall grid size. The total grid size was: 4425 cells, 8059 faces and 4081 nodes. The single-channel simulation total grid size was considerably smaller (about 81% smaller) than the full 2-D grid (26017 cells, 45283 faces and 19172 cells).

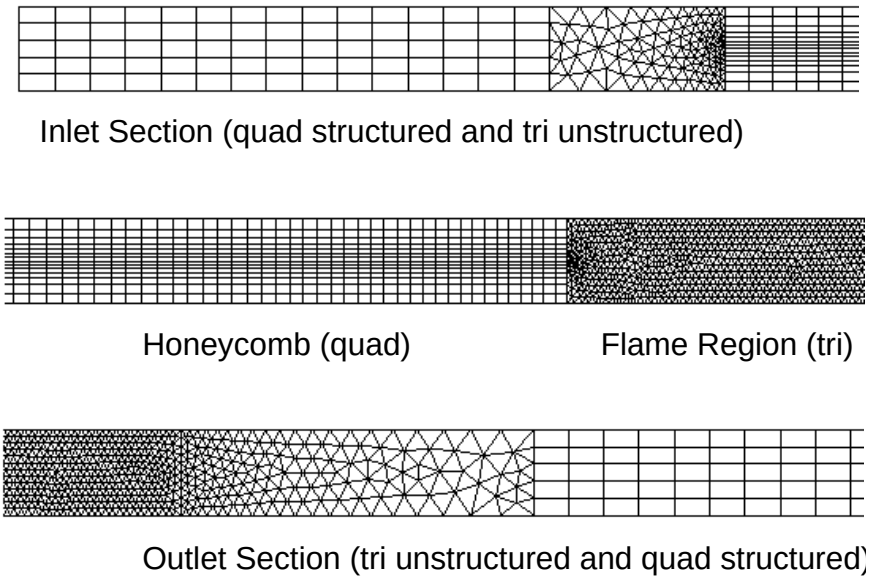

Figure 6.2: Single channel grid: inlet, honeycomb, flame and outlet sections

6.2.2 Boundary Conditions

Mass flow boundary condition provides a prescribed mass flow rate or mass flux distribution at an inlet. Physically, specifying the mass flux permits the total pressure to vary in response to the interior solution. A mass flow inlet is often used when it is more important to match a prescribed mass flow rate than to match the total pressure of the inflow stream. For the Rijke tube simulation (see Chapter 4), it was necessary to maintain a pressure anti-node at the inlet and therefore using the velocity inlet was the correct option. When the mass flow boundary condition is implemented at an inlet, a velocity is computed, and this velocity is used to compute the fluxes of all relevant solution variables into the domain. With each iteration, the computed velocity is adjusted so that the correct mass flow value is maintained. Once the mass flow rate ($\dot{m}$) or the mass flux (mass flow rate per unit area, $\rho v_n = \dot{m}/A$) is specified, the density, ρ, at the face must be determined in order to find the normal velocity, v_n.

If the fluid is an ideal gas, the static temperature and static pressure are required to compute

the density:

$$\rho = \frac{p}{RT} \tag{6.1}$$

Since the inlet is subsonic, the static pressure is extrapolated from the cells inside the inlet face. In low-Mach-number compressible flow, the overall pressure drop is small compared to the absolute static pressure, and can be significantly affected by numerical roundoff. To understand why this is true, consider a compressible flow with $Ma << 1$. The pressure changes, Δp, are related to the dynamic head, $\frac{1}{2}\gamma p Ma^2$, where p is the static pressure and γ is the ratio of specific heats. This gives the simple relationship $\Delta p/p \approx Ma^2$, so that $\Delta p/p \to 0$ as $Ma \to 0$. Therefore, unless adequate precaution is taken, low-Mach-number flow calculations are very susceptible to roundoff error. Therefore, by using the mass-flux inlet boundary condition, we can insure that the overall mass flow rate does not get affected by incorrect inlet pressure prediction (and consequently density calculation).

The mass flux inlet boundary condition that has been applied at the computational inlet consists of a mean component ($\overline{[\rho v_n]}$, where v_n is velocity normal to the inlet boundary) and a fluctuating component ($[\rho v_n]'$). The total mass flux, at a given time (t) and for a frequency of excitation (ω), is computed as:

$$[\rho v_n] = \overline{[\rho v_n]}\,[1 + 0.1\sin(2\pi\omega t)] \tag{6.2}$$

where, $[\rho v_n]' = 0.1\overline{[\rho v_n]}\sin(2\pi\omega t)$. The outlet boundary is at atmospheric pressure ($p' = 0$).

Periodic boundaries have been used since the physical geometry of interest and the expected pattern of the flow/thermal solution have a periodically repeating nature. FLUENT treats the flow at a periodic boundary as though the opposing periodic plane is a direct neighbor to the cells adjacent to the first periodic boundary. Thus, when calculating the flow through the periodic boundary adjacent to a fluid cell, the flow conditions at the fluid cell adjacent to the opposite periodic plane are used. The boundary conditions have been summarized in Table 6.1.

Table 6.1: Boundary conditions for the single channel flat flame simulation

Boundary	Boundary Condition
Computational Inlet	Uniform mass-flux profile with imposed $[\rho v_n]'$ sinusoidal oscillations from $15\,Hz$ to $500\,Hz$
Outlet (Open)	Atmospheric pressure ($p' = 0$)

6.2.3 Flow, Chemistry and Heat Transfer Modeling

Second order accurate schemes have been used for discretization of velocity, density, energy and species terms. The SIMPLE algorithm has been applied for pressure-velocity coupling and a second order accurate interpolation scheme has been used for pressure. A second order accurate temporal integration scheme has been used in the computations.

The two-step methane-air reaction model (see section 5.4.3) from the full 2-D study has been retained (described in section 5.4.3).

Radiation Modeling

In the full 2-D simulation, the Discrete Ordinates (DO) method was used for radiation modeling. The DO model is capable of calculating radiative heat exchange in the presence of both optically thick and optically thin participative media. Therefore, it is a computationally expensive model to implement. While making the assumption that the post-flame combustion products are optically thin, the DO model is able to predict the radiation losses accurately in the full 2-D simulation. However, Lammers and Goey [93] have shown that the optically thin limit overestimates the temperature gradient in the flue gases and the error is more than 10% for a mean beam length of approximately $1\,cm$. The authors using a numerical model and experimental results showed that the volume of the hot combustion products can be represented by a cone with a base diameter equal to the burner diameter and a height

approximately two times the burner diameter. The mean beam length (L_e) is then given by:

$$L_e \approx \frac{8}{15} d \tag{6.3}$$

where, d is the diameter of the flat flame burner. In the present study, $L_e \approx 3.79\,cm$. Therefore, the optically thin assumption for the combustion products introduces errors in the radiative heat exchange calculations. Although, the DO radiation model accounts for optically thick participative medium, it can be replaced by a computationally inexpensive radiation model that is able to account for optically thick media. The P-1 model is therefore chosen in this part of the study to reduce the computational expense even further. The P-1 radiation model [94] is the simplest case of the more general P-N model, which is based on the expansion of the radiation intensity into an orthogonal series of spherical harmonics. The radiation flux (q_r) in the model is computed as:

$$-\nabla q_r = aG - 4a\sigma T^4 \tag{6.4}$$

where, a is the absorption coefficient, σ is the Stephan-Boltzmann constant and G is the irradiation. The expression for $-\nabla q_r$ can be directly substituted into the energy equation to account for heat sources (or sinks) due to radiation.

6.3 Reacting Flow Results

Results for the single channel flat flame simulation are presented in this section. A case study with flow rate of $Q = 200\,cc/s$ and equivalence ratio of $\phi = 0.75$ has been modeled. It will be shown that the results compare favorably with the full two-dimensional study that were described in chapter 5. First the reacting flowfield will be described followed by the FRF and lastly some of the dynamic characteristics of the flat flame are presented.

6.3.1 Reacting Flowfield Structure

The steady state result for the single channel simulation was obtained substantially faster compared to the full two-dimensional simulation. The steady state solution converged in less than 2000 iterations after the air-fuel mixture was ignited. This is a factor of two faster than the full two-dimensional simulation. Also, the computation time needed was drastically lower, primarily because of the lower number of grid points in the single channel computational domain.

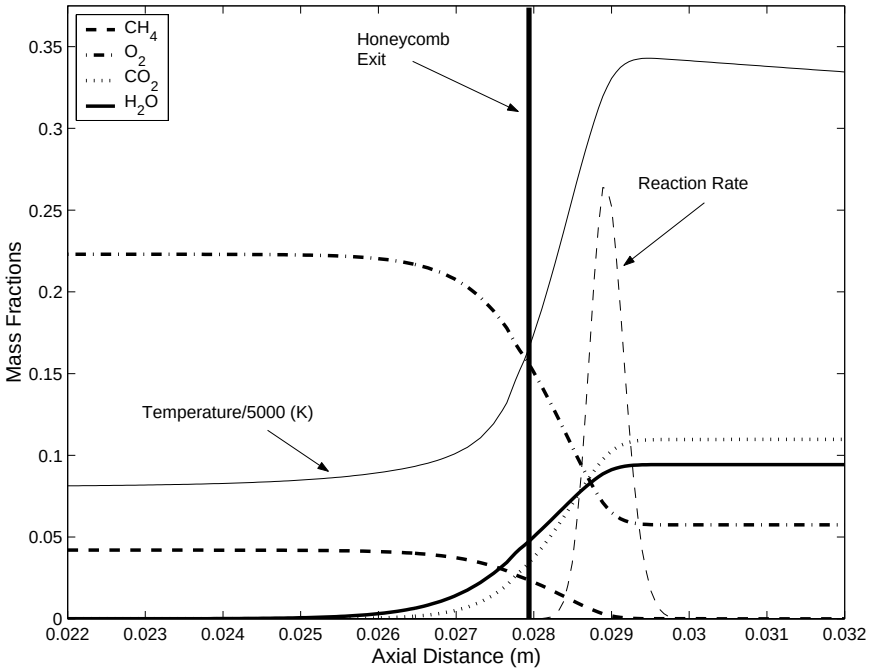

Figure 6.3: Axial variation of mass fractions of CH_4, O_2, CO_2 and H_2O in the single channel for $Q = 200\,cc/s$ and $\phi = 0.75$. Temperature (K) and reaction rate variations are also shown.

After the steady state solution is reached, the unsteady solver of FLUENT was applied to compute time integration without exciting the flame with inlet mass-flux oscillations. Time averaged axial variation of mass fractions of CH_4, O_2, CO_2 and H_2O are shown in Figure 6.3. The reaction rate curve shown in the figure indicates that the flame anchors $1\,mm$

downstream of the honeycomb exit. This is in agreement with the flame location from the full two-dimensional study. The axial variation of temperature can also be observed in the figure. The temperature peaks immediately downstream of the reaction rate peak and then decreases further downstream. It should be noted here that the temperature distribution upstream of the flame is predicted correctly in this part of the study as compared to the distribution calculated in the full 2-D study (see Figure 5.10). The possible reason for this difference is the absence of a fine grid in the full 2-D simulation. The flame thickness calculated for this study has been found to lie in the range predicted by correlations for premixed, preheated flames (approximately $1\,mm$ to $3\,mm$ range).

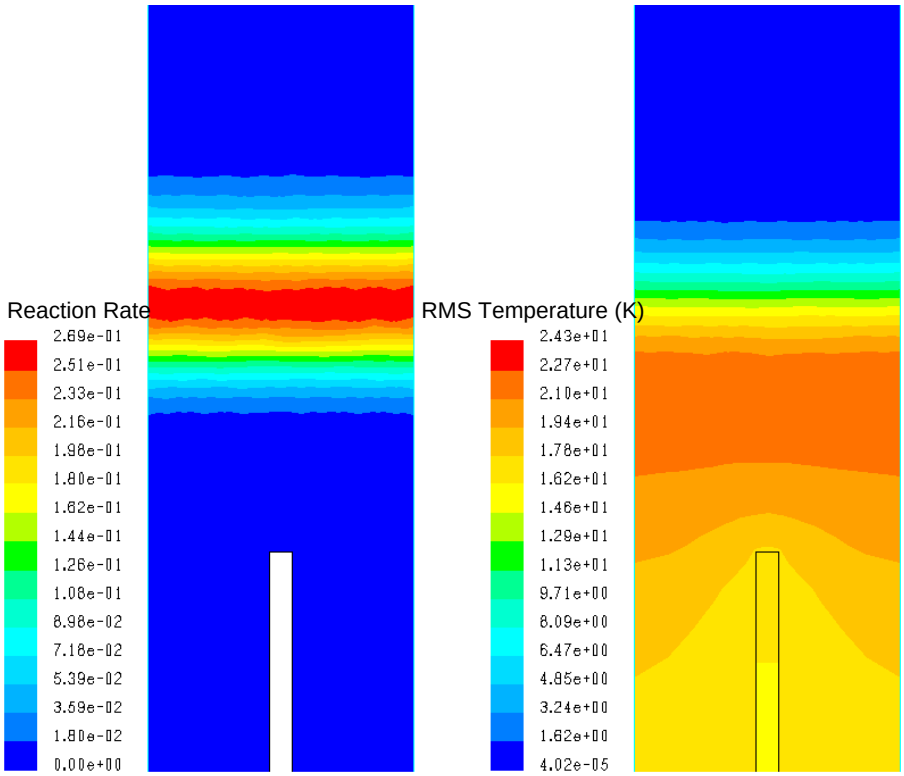

Figure 6.4: Contours of RMS temperature shown relative to mean value of reaction rate contours inside the single channel for $Q = 200\,cc/s$ and $\phi = 0.75$

The flame position can also be seen in Figures 6.4 and 6.5 along with RMS temperature and

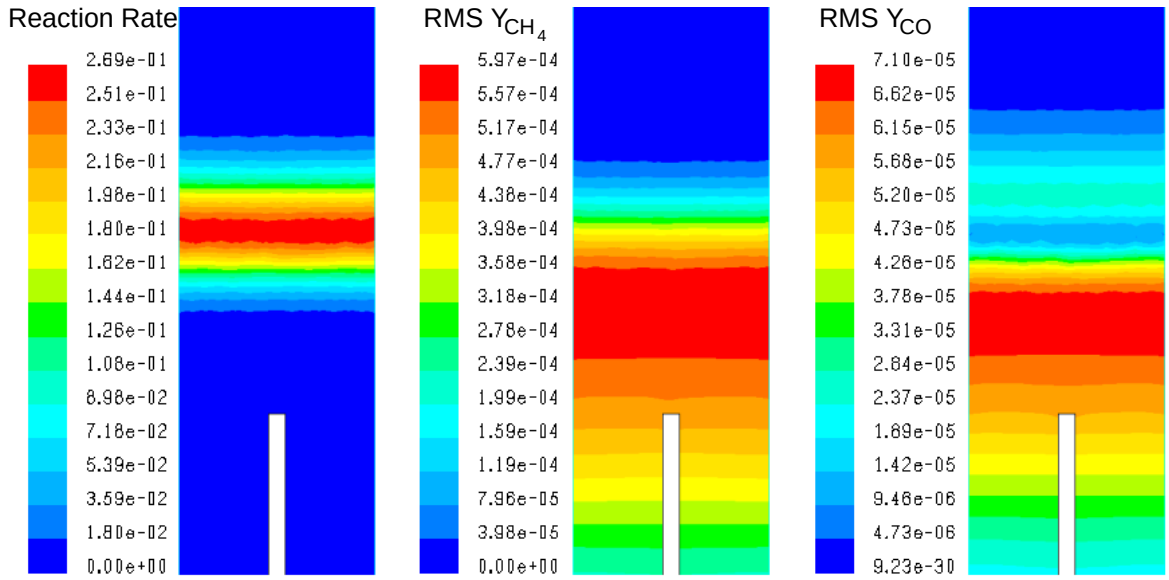

Figure 6.5: Contours of RMS mass fractions of CH_4 and CO shown relative to mean value of reaction rate contours inside the single channel for $Q = 200\,cc/s$ and $\phi = 0.75$

RMS species mass fractions of CH_4 and CO. It can be observed in Figure 6.5 that the RMS fluctuations in temperature and species mass fractions peak immediately upstream of the flame inner reaction zone. Since CH_4 is not present downstream of the flame, RMS fluctuations of CH_4 mass fraction is zero downstream of the flame. However, CO is present downstream of the flame and therefore RMS fluctuations in its mass fractions can be observed. The fluctuations die down immediately downstream of the flame though. It was observed that the mean flame position remains the same irrespective of the excitation frequency. RMS temperature and species mass fractions also peak at the same location irrespective of the excitation frequency. However, their peak values are dependent on the excitation frequency.

6.3.2 Frequency Response Function

The FRF was computed from time traces of integrated reaction rate and fluctuating velocity. The procedure was the same as explained in section 5.5.2. The FRF is shown in Figure 6.6. It

can be observed in the magnitude plot that the low frequency resonance has been captured by the CFD model. The magnitude at the low frequency resonance ($30\,Hz$) is approximately $8\,dB$. At $500\,Hz$ the magnitude decreases approximately $45\,dB$ per decade indicating a second order system (2 poles). To get a good match with the data points, a third order fit (3 poles and 1 zeros) has been applied to obtain the transfer function. The associated FRF phase is also shown in Figure 6.6. A phase drop of 180° can be observed between $15\,Hz$ and $50\,Hz$) indicating that the system is lightly damped.

The pole-zero plot is shown in Figure 6.7. The transfer function comprises of two real poles (666.13 and -0.46), a pair of complex conjugate poles ($5.56 \pm 29.64i$) and two real zeros (976.2161 and -0.5648). Since all four poles lie on the left hand plane, the open-loop system is stable. The stability of the corresponding closed-loop system can be investigated by calculating the gain margin and the phase margin angle.

A comparison of the single channel CFD model with the full two-dimensional simulation shows that the single channel model is able to capture the low frequency instability that the two-dimensional model failed to capture. Figure 6.8 shows the comparison between the two CFD models and the FRF from the experiment [1]. As can be observed, the single channel CFD model has been successful in predicting the low frequency resonance phenomenon that was observed in experiments. The resonant frequency was computed to be approximately $30\,Hz$ as compared to $32.5\,Hz$ found in the experimental study. There can be many reasons attributed to the difference in the resonant frequency between the CFD result and experimental data. One possible reason can be the use of approximate values of thermophysical properties of cordierite (the honeycomb material). In particular, the thermal conductivity of cordierite was assumed to not vary with temperature. Although, in the radial direction, the effect of constant thermal conductivity would not have affected the solution, the axial variation would probably alter the resonant frequency obtained by the CFD model. Further investigation of the effect of heat transfer on the resonant frequency is discussed in section 6.4.

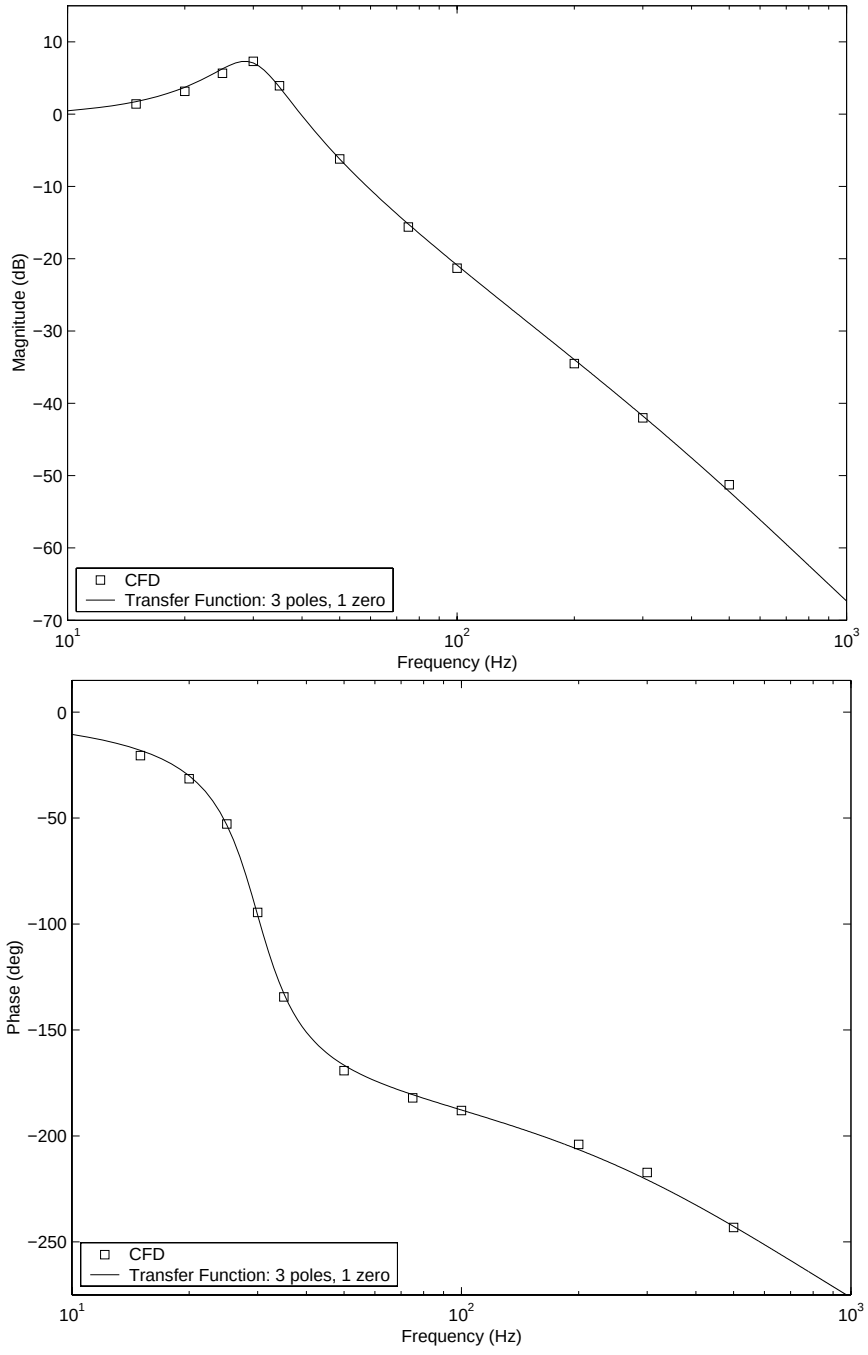

Figure 6.6: Single channel frequency response function magnitude and phase (CH_4-air, $Q = 200\,cc/s$ and $\phi = 0.75$)

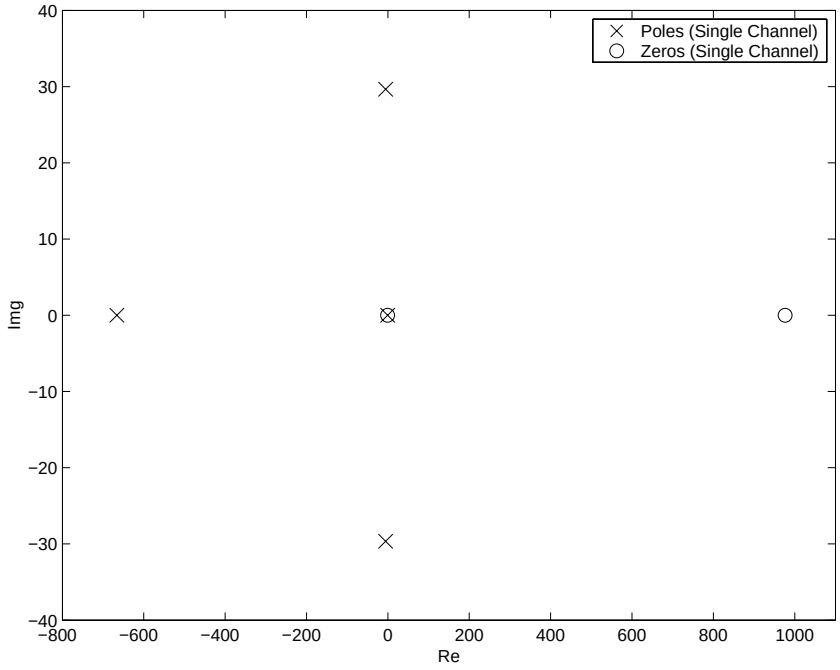

Figure 6.7: Single channel frequency response function pole-zero plot ($Q = 200\,cc/s$ and $\phi = 0.75$)

From the magnitude plot in Figure 6.8 it can also be observed that the rolloff at higher frequencies in the single channel CFD model case is approximately $45\,dB$ per decade (indicating a 2nd order system) and is close to that of the experimental curve.

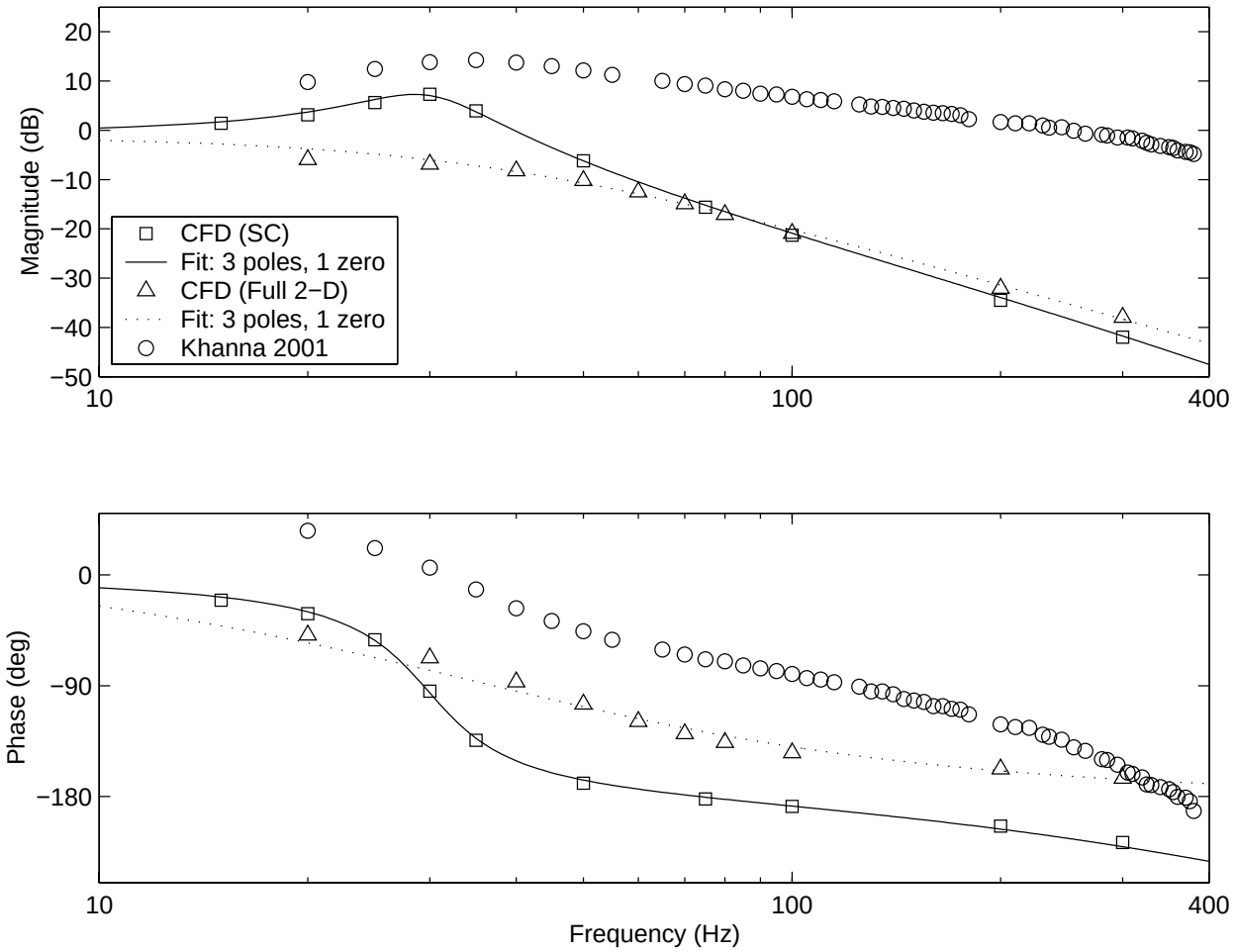

Figure 6.8: Comparison of frequency response function between full two-dimensional CFD study and the single channel CFD study. Experimental data [1] has been included for comparison with the CFD results

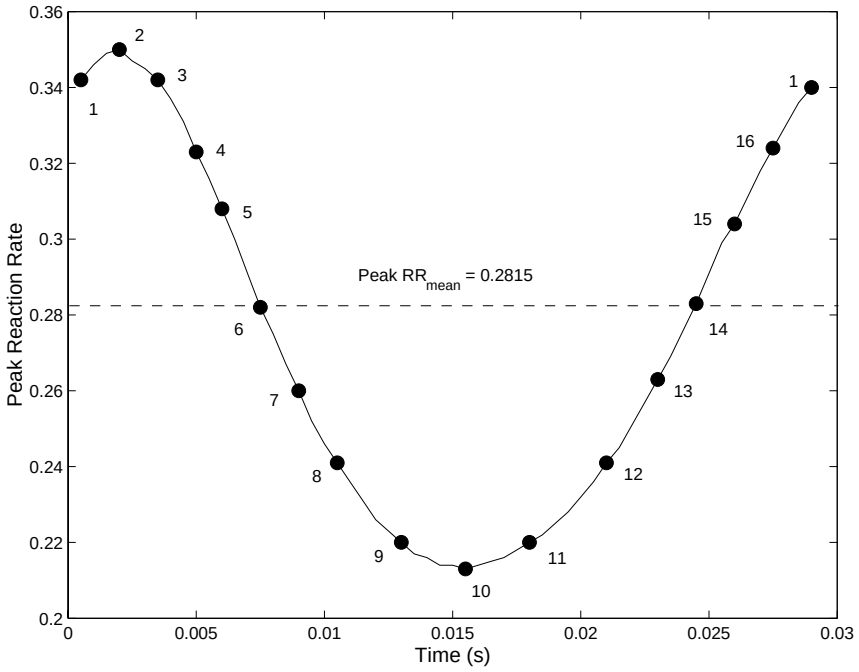

Figure 6.9: Peak reaction rate variation at $35\,Hz$ inside the single channel flat flame. Snapshots of reaction rate iso-contours are shown in Figure 6.10 corresponding to the circles marked on the peak reaction rate curve. The mean peak reaction rate is 0.2815 ($kgmol/m^3$-s) which corresponds to $RR' = 0$

6.3.3 Dynamic Characteristics of the Flat Flame

Fleifel et al. [2] showed that the flat flame heat release rate is directly proportional to its area change. This phenomena is also observed in the single channel CFD simulation. The flat flame is seen to oscillate on top of the honeycomb flame stabilizer. The flame shows complex dynamics in terms of its thickness and position. Figure 6.9 shows the variation of peak reaction rate inside the flame. The peak reaction rate reaches a minimum value around $0.015\,s$ and has a mean value of 0.2815 ($kgmol/m^3$-s). The variation of the peak reaction rate has been shown for the $35\,Hz$ excitation case which is close to the resonance frequency of $30\,Hz$. The solid circles in the figure are where snapshots of the flame have been recorded and are shown in Figure 6.10. The following symbols have been used in Figure 6.10 to

describe flame shape and location:

- solid red circle – location where reaction rate peaks
- red circle with blue border – flame bottom surface location
- blue circle with red border – flame top surface location

Using these symbols we can explain the dynamics of flame shape and position. We can observe from the figure that as the velocity peaks, the reaction rate goes up and consequently the flame flashes back toward the honeycomb. As the flame nears the honeycomb its thickness reduces. This happens because of the following relationship:

$$l_F \propto \frac{1}{S_L^2} \tag{6.5}$$

where, l_F is the flame thickness and S_L is the laminar flame speed. If we start from position 1 (snapshot number 1) and move toward position 16, we can understand how the flame behaves. At $35\,Hz$, the velocity (measured at the computational inlet) leads the reaction rate by approximately 150°. Therefore, the peak reaction rate is reached after velocity upstream of the flame has peaked. As the velocity increases, the laminar flame speed also increases. Consequently, the flame thickness decreases. As the velocity goes down, the flame tends to move away from the honeycomb since the reaction rate is also decreasing. This movement of the flame can be noticed in Figure 6.10. The flame is the thickest in position 12 whereas the reaction rate (and therefore S_L) has a minimum at position 10 (see Figure 6.9 for reaction rate minimum). A time delay is present in the system that makes the flame shape change out of phase with the reaction rate. Figure 6.11 shows the mean flame position, flame thickness and peak reaction rate changing with time. The flame thickness reaches its maximum $5.5\times10^{-3}\,s$ after the reaction rate reaches its minimum. The flame thickness varies between $1.22\,mm$ and $1.46\,mm$ with a mean value of $1.331\,mm$. The flame location is the furthest from the honeycomb $2\times10^{-3}\,s$ earlier compared to when the flame is the thickest. The flame position changes between $1.237\,mm$ and $1.627\,mm$. The total time delay between

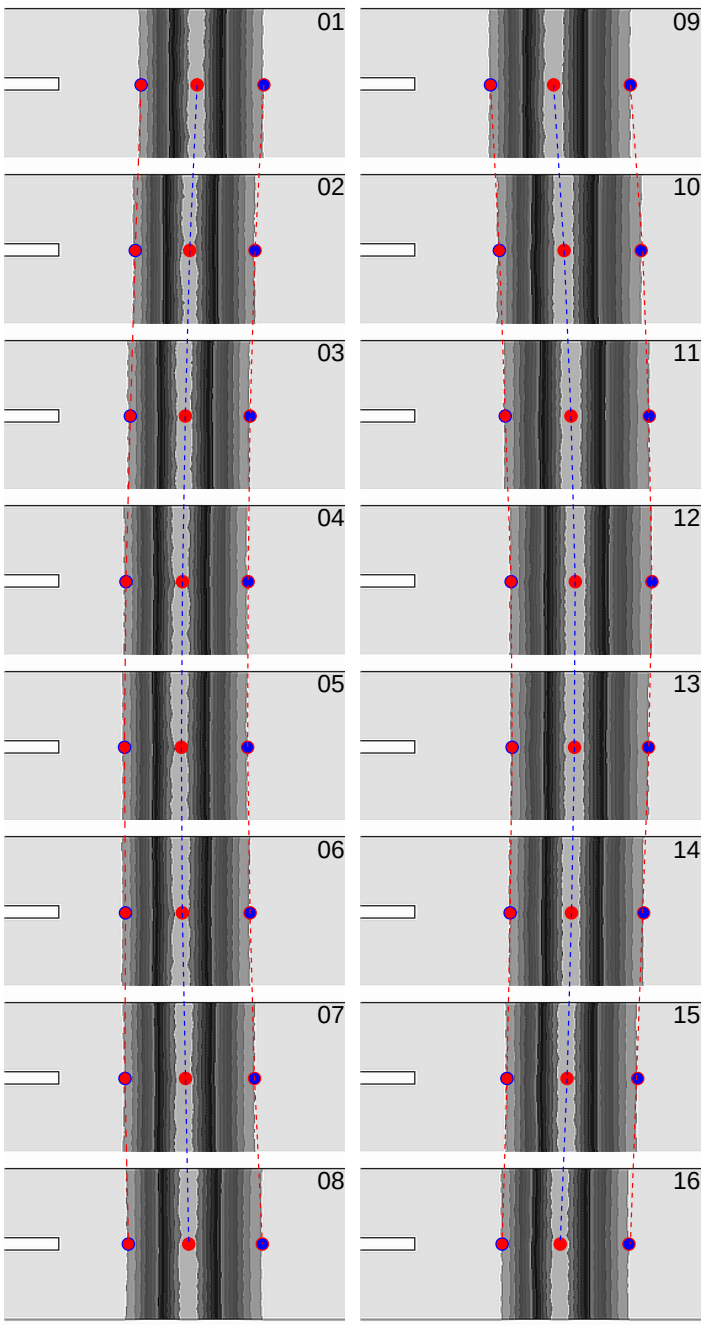

Figure 6.10: Snapshots of reaction rate iso-contours showing flame movement at $35\,Hz$ for the single channel simulation. The numbers on each snapshot corresponds to the circles shown in Figure 6.9

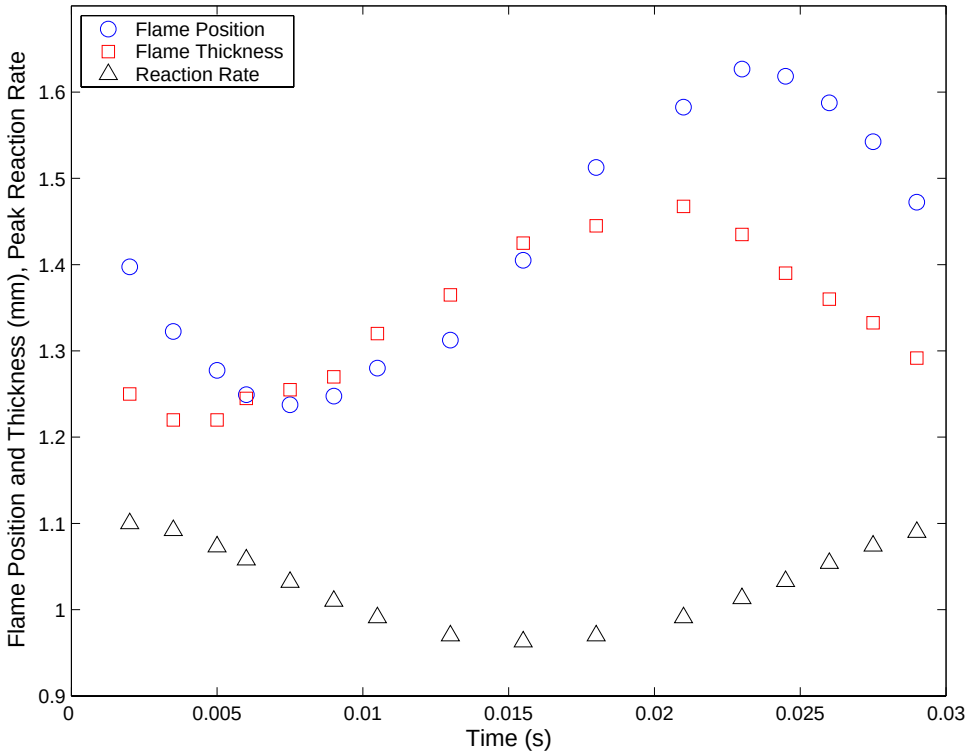

Figure 6.11: Change in flame position, flame thickness and peak reaction rate with time (35 Hz excitation) for the single channel simulation. The flame position is calculated from the solid red circle locations in Figure 6.10 and corresponds to the peak reaction rate location. The reaction rate shown corresponds to the peak reaction rate plus 0.75 $kgmol/m^3$-s

reaction rate minimizing and flame position furthest away from the honeycomb, therefore, is $7.5 \times 10^{-3}\, s$.

6.4 Investigation of the Low Frequency Resonance

The resonance phenomenon that was observed in the FRF between q' and u' (see section 6.3.2) will be investigated in this part of the flat flame burner study. It is important to

understand the physical reasoning behind the resonance since it has been shown that such pulsating instabilities in presence of large scale heat transfer can cause growth of thermoacoustic instabilities. The resonance which occurred at $30\,Hz$ was also observed in power

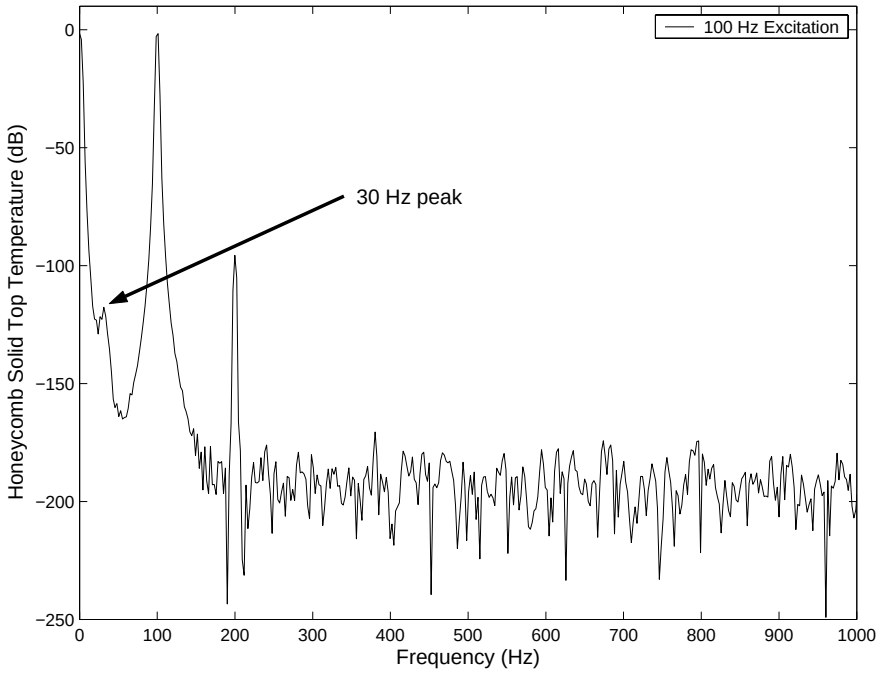

Figure 6.12: Honeycomb top temperature power spectrum for $100\,Hz$ excitation case (single channel simulation). The $30\,Hz$ resonant frequency is visible in the spectrum

spectrum of reaction rate and temperature irrespective of the frequency of excitation. In Figures 6.12 and 6.13 the $30\,Hz$ peak is distinctively visible even though the frequency of excitation was $100\,Hz$. It can be argued that the presence of the $30\,Hz$ peak is an indication of transients, since resonant frequencies tend to show up.

The presence of the peak in the honeycomb top temperature power spectrum (Figure 6.12) confirmed the role of heat transfer coupling between the flame and the honeycomb. To investigate the resonance phenomenon, therefore, it was decided to concentrate on the role of heat transfer in the reacting flow. The decision was based on observations made earlier by investigators (see Buckmaster [71] and Khanna [1]) showing that the heat transfer coupling

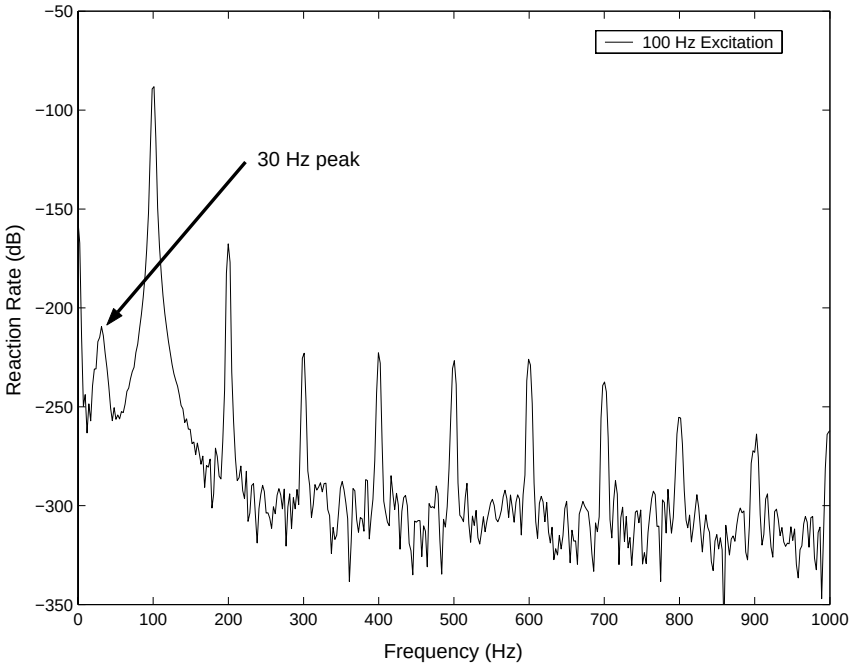

Figure 6.13: Reaction rate power spectrum for $100\,Hz$ excitation case (single channel simulation). The $30\,Hz$ resonant frequency is visible in the spectrum

between the flat flame and the flame stabilizer (the honeycomb in the present study) was responsible for the resonance phenomenon. The authors did not offer a physical explanation for the phenomenon. Khanna [1] showed that conduction heat transfer between the flame and the honeycomb is important, although convection heat transfer is not. The reasoning that was offered was based on the assumption that the convective heat transfer coefficient inside the honeycomb fluid channels remains unaffected by the oscillating mass-flux through the channels. Buckmaster [71] used perturbation analysis to show that the pulsating instability is caused because of a time-delay between preheating of the incoming mixture and the heat release from the flame.

Both Buckmaster's work and Khanna's observations indicate the role of heat transfer in causing the physical phenomenon. In this part of the study it was, therefore, assumed that the flame plays the role of a heat source and the influence of chemistry on the resonance

is minimal. Having established the criterion of not involving chemical kinetics in the CFD study, it was decided to replace the flame with a heat source. The study has been divided into two parts – the first part involves replacing the flame with a constant heat source and evaluating the effect on the heat transfer between the source and the honeycomb whereas the second part of the study involves using a time varying (oscillating) heat source and investigating its effect on the heat transfer.

The CFD model from the reacting flow simulation was retained and only the chemistry modeling was excluded. Second order discretization in space for momentum, density and energy, second order interpolation for pressure, the SIMPLE algorithm for pressure-velocity coupling and the P-1 model for radiation modeling were retained. Air was considered to be the fluid flowing with its properties calculated using the ideal gas law (density) and from kinetic theory of gases (C_p, k, μ).

6.4.1 Effect of Constant Heat Source

A volumetric heat source was applied to the flame region. The heat source power density ($\dot{Q} = 7.5 \times 10^6\, W/m^3$) was selected such that the mean temperature distribution obtained followed the mean temperature distribution from the reacting flow solution. A comparison between the temperature profile obtained from the reacting flow case and the constant heat source case is shown in Figure 6.14. The temperature profiles inside the honeycomb are slightly different because of the difference between the thermal conductivity of air ($1.2 \times 10^{-2}\, W/m\text{-}K$) and the CH_4-air mixture ($3.25 \times 10^{-2}\, W/m\text{-}K$). Variation of the thermal conductivities inside the honeycomb channel is shown in Figure 6.15.

The maximum temperature in the constant heat source case is $400\, K$ higher than the reacting flow case ($T_{max,reacting} \approx 1700\, K$). Also, the temperature decrease in the reacting flow solution is steeper than the non-reacting flow case. The difference is because of the presence of CO_2 and H_2O in the reacting flow case. CO_2 and H_2O have dipole moments and therefore absorb more radiation as compared to air which comprises of O_2.

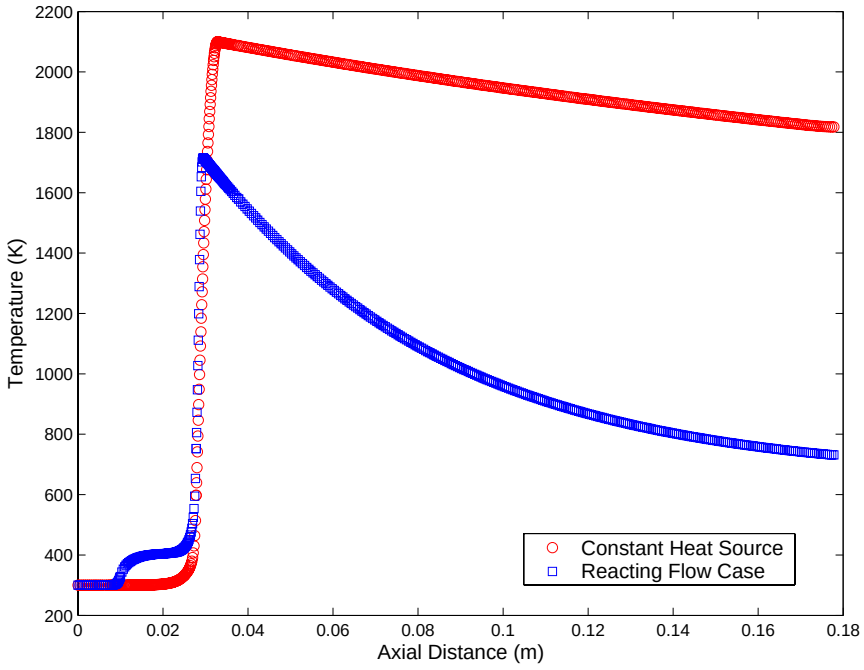

Figure 6.14: Mean temperature variation in the single channel for the constant heat source case and the reacting flow $0\,Hz$ excitation case

Frequency Response of Honeycomb Temperature

To obtain an FRF between fluctuating components of temperature and velocity, the incoming air was oscillated sinusoidally. The FRF magnitude obtained between the honeycomb top solid temperature T'_{solid} and u' is shown in Figure 6.16 and between the honeycomb exit fluid temperature T'_{fluid} and u' is shown in Figure 6.17. The FRF magnitude decreases between $15\,Hz$ and $100\,Hz$ and does not show any dynamics similar to the resonance observed in the reacting flow case near $30\,Hz$. The constant heat source case, therefore, shows first order dynamics and does not support the role of heat transfer in creating the low frequency resonance at $30\,Hz$.

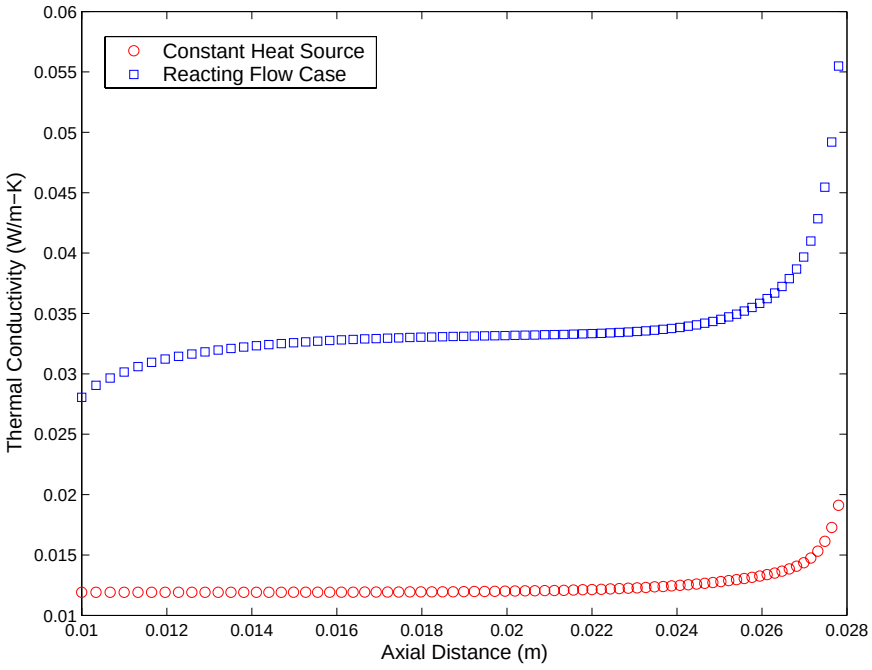

Figure 6.15: Thermal conductivity variation inside the honeycomb for the constant heat source case and the reacting flow $0\,Hz$ excitation case (single channel simulation)

6.4.2 Effect of Time Varying Heat Source

The resonance phenomenon observed at $30\,Hz$ in the reacting flow simulation of the flat flame can be replicated in the heat transfer study only if a second order system can be created. The presence of a constant, time invariant heat source in the previous attempt did not change the order of the system, even though the incoming mass flux oscillate sinusoidally. The purpose of this part of the study is to introduce a time varying heat source that replaces the flame in the reacting flow simulation. This time varying heat source creates a second order system that shows a resonance condition.

McIntosh and Clarke [95] showed that for any arbitrary Lewis number, the heat conduction to the flame holder can have important second order effects. The flame holder for the planar

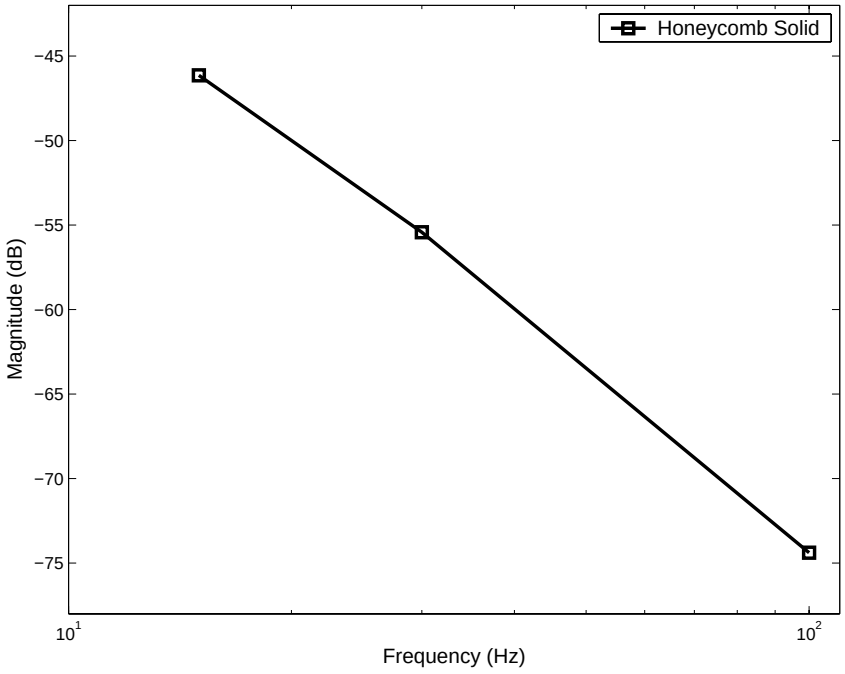

Figure 6.16: FRF magnitude between the normalized honeycomb top solid temperature and normalized velocity $T'_{solid}/\overline{T}_{solid}$ and $u'/\overline{u}$ for the constant heat source case

flame was represented by a δ-function heat sink situated within the inert pre-heat domain and the flame stand-off distance was defined as the distance between the flame sheet and the heat sink. The authors found that for Lewis numbers close to unity (e.g. lean CH_4-air mixture), a planar instability of the burner flames depends not only on stand-off distance (and thus heat loss) but on the magnitude of the activation energy. McIntosh [96] subsequently described the role of heat transfer in causing the low frequency resonances. It was shown that the driving mechanism for the oscillations is fluctuating heat transfer to a gauze anchoring the flame. It was argued that the heat transfer modes were actually the 'natural frequency modes' of the system when the stand-off distance was finite (connected to the heat loss to the gauze). The conclusion of the study was that for any value of Lewis number, tube length and finite stand-off distance, there exist a number of resonant frequencies which are associated with the stand-off distance. These are not 'tube' modes, but rather specifically

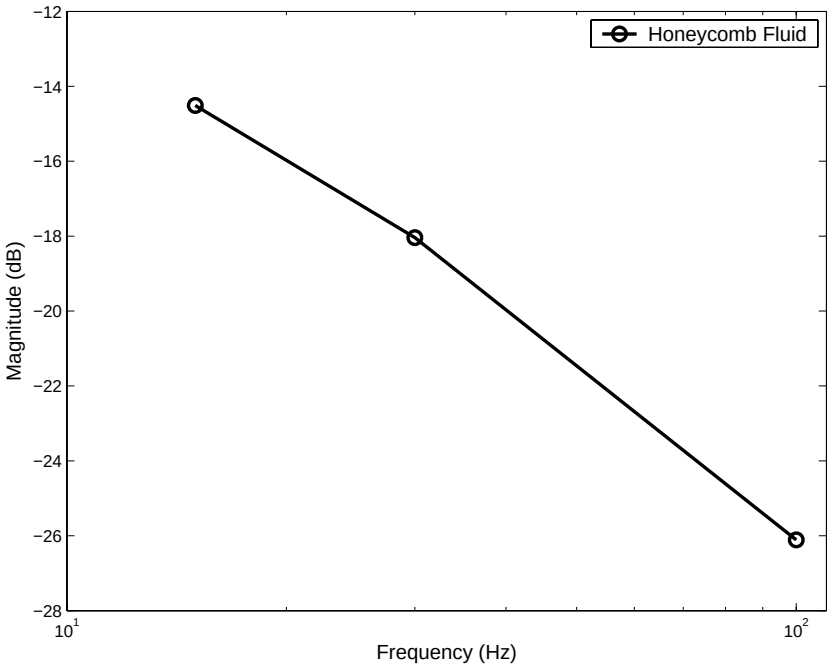

Figure 6.17: FRF magnitude between the normalized honeycomb exit fluid temperature and normalized velocity $T'_{fluid}/\overline{T}_{fluid}$ and $u'/\overline{u}$ for the constant heat source case

represent heat losses associated with resonance. For a given tube length, there is a range of stand-off distances for which each mode will have linear instability.

Artyukh et al. [97] studied the effects of instantaneous and periodic perturbations in mass flow rate on a laminar premixed non-adiabatic flame. Second and third order dynamical linearized models were solved analytically and numerically. Influence of radiation and heat losses to the burner were investigated. Linear stability analysis was performed for the laminar flame and forced oscillations of the incoming air-fuel mixture was imparted. To create a second order system the burner temperature was also pulsated sinusoidally:

$$T_b = T_{b_1}[1 + A_1 \cos(\omega_1 t)] \tag{6.6}$$

and a second order equation was obtained:

$$\ddot{\xi_1} + \sigma\dot{\xi_1} + \Delta\xi_1 = A_1 \cdot f \cdot \cos(\omega_1 t) \tag{6.7}$$

where $\xi = C - C_s$ is a small deviation of the mass flow rate from steady state value C_s. Solving this equation with initial conditions, the authors determined the frequency of the undamped natural oscillations and the damping coefficient of the natural damped oscillations as well as the amplification factor, amplitude and phase angle of the forced oscillations. It was established that the system is sensitive to the damping coefficient in the vicinity of the resonance. In lightly damped systems (like the flat flame burner system from our reacting flow study), the amplification has a maximum value at a frequency close to the resonance frequency.

From the studies of McIntosh and Clarke [95], McIntosh [96] and Artyukh et al. [97], it is clear that there are two requirements that are necessary to create a heat transfer model that mimics the heat transfer interaction between the flame and the honeycomb:

1. The model should be able to replicate the temperature gradients observed in the flat flame reacting flow simulation to capture the 'jump condition' [96] at the flame and the creation of a preheat 'inert zone' [95] as seen in burner stabilized flame, and

2. at least a second order system must be created for resonance to occur.

The first requirement was met in the constant heat source study described earlier. The second requirement, however, was not met because, unlike in the study of Artyukh et al. [97], a second source (e.g. oscillating burner temperature) was not present in the constant heat source case. By introducing a second oscillating source in the heat transfer model, it is aimed to create a second order system that mimics the heat transfer dynamics of the flat flame reacting flow simulation. Instead of creating a oscillating burner temperature source, the heat source itself is to be oscillated. The oscillating heat source creates a heat transfer coupling with the honeycomb that will create an oscillation in the honeycomb temperature. The mean volumetric heat source is kept constant at $\overline{\dot{Q}} = 7.5 \times 10^6\, W/m^3$ and the instantaneous volumetric source is computed as:

$$\dot{Q} = \overline{\dot{Q}}\,[1 + 0.1\sin(2\pi\omega t - \varphi)] \tag{6.8}$$

where φ is the phase difference between the mass-flux oscillation at the computational inlet and the oscillating volumetric heat source. The phase angle was taken from the reacting flow simulation (e.g. at $100\,Hz$ the phase was approx. $-125°$). Figure 6.18 shows the temporal variation of the honeycomb solid top temperature. This variation of the honeycomb top temperature is caused by the unsteady heat source sitting downstream of the honeycomb exit.

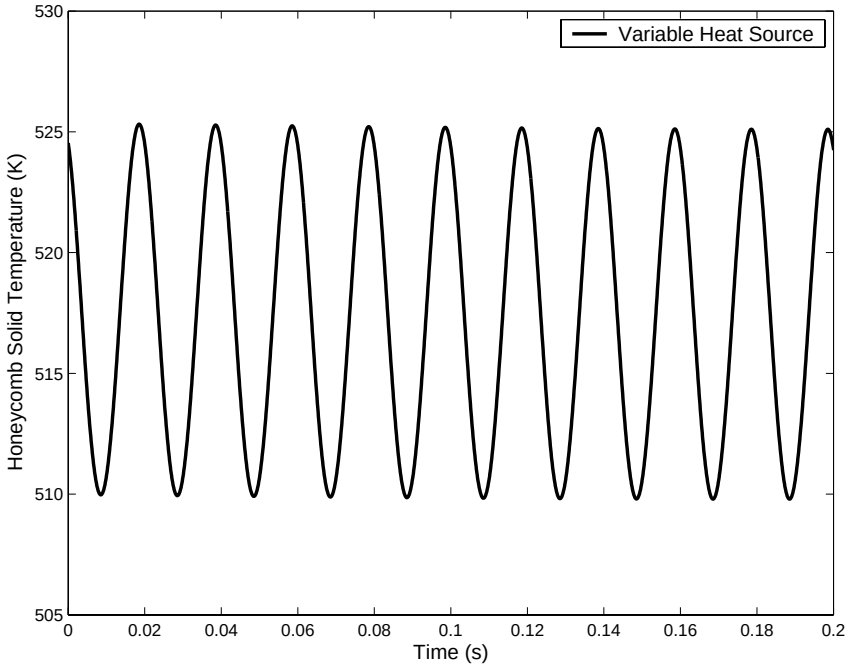

Figure 6.18: Temporal variation of the honeycomb top solid temperature for the time varying heat source case ($35\,Hz$ excitation, single channel simulation)

Frequency Response of Honeycomb Temperature

Upon oscillating the heat source at different frequencies out of phase with the incoming velocity fluctuations, frequency response of the honeycomb exit plane temperatures were obtained. The magnitude of T'_{solid} with respect to the upstream u' is shown in Figure 6.19. A distinct peak at $30\,Hz$ is visible in the figure. This resonant peak indicates that the natural

frequency of the system lies around $30\,Hz$. The natural frequency predicted by this heat transfer model matches closely with the experimentally observed resonant peak of $29\,Hz$ and the resonance peak predicted by the single channel reacting flow CFD model ($30\,Hz$).

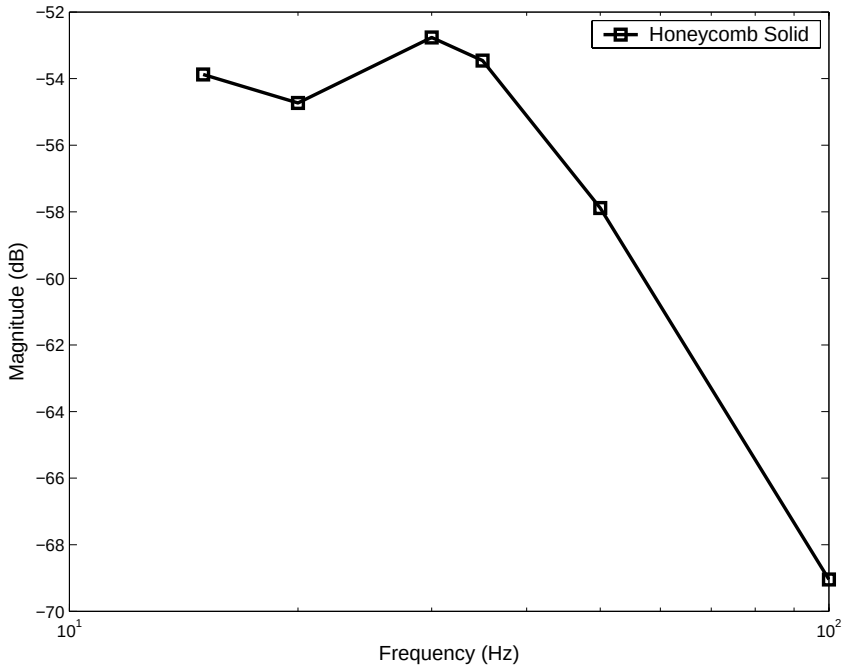

Figure 6.19: FRF magnitude between the normalized honeycomb top solid temperature and normalized velocity $T'_{fluid}/\overline{T}_{fluid}$ and $u'/\overline{u}$ for the time varying heat source case

The observed resonance (between $30\,Hz$ and $35\,Hz$) in the honeycomb solid temperature is also seen in the honeycomb outlet fluid temperature (see Figure 6.20). For the honeycomb solid temperature, the increase in magnitude of oscillation is approx. $2\,dB$ between $20\,Hz$ and $30\,Hz$ and the overall oscillation magnitude drop is from $-53\,dB$ to $-69\,dB$ between $30\,Hz$ and $100\,Hz$. The increase in honeycomb solid temperature is small as compared to the magnitude increase observed between $15\,Hz$ and $30\,Hz$ in the honeycomb fluid temperature (approx. $6\,dB$). The heat transfer between the heat source and the honeycomb solid primarily occurs because of conduction (resulting from a temperature gradient). The solid has more inertia and is resistant to any changes in the downstream change of the temperature

gradient and, therefore, shows less change in fluctuation magnitude. This small oscillation magnitude though has a profound effect on the convective heat transfer coefficient in the honeycomb channel and results in a higher convective heat transfer rate between the honeycomb solid and the incoming fluid. Previous work in heat transfer studies – natural/forced convection – have shown that the unsteady heat transfer coefficient shows an increase in the case of pulsating flow and in the presence of oscillating heat sources [98, 99, 100, 101].

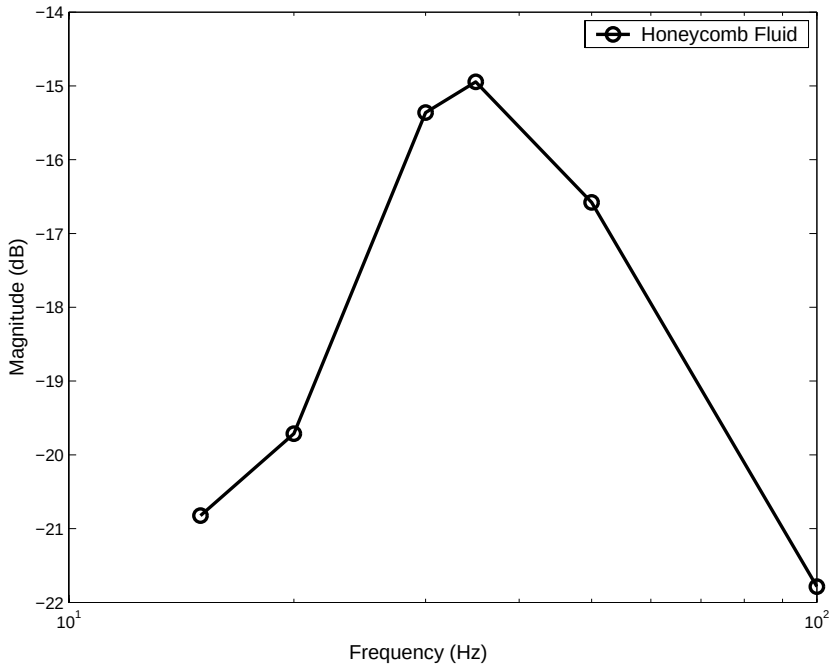

Figure 6.20: FRF magnitude between the normalized honeycomb exit fluid temperature and normalized velocity $T'_{solid}/\overline{T}_{solid}$ and $u'/\overline{u}$ for the time varying heat source case

The resonant peak near $30\,Hz$ observed for the honeycomb exit fluid temperature proves that the thermal boundary layer is excited by the mass-flux oscillations and the oscillation in the heat source downstream of the honeycomb. The increase in the fluid temperature can only occur due to convection heat transfer – conduction from the downstream heat source does not contribute significantly. It can therefore be argued that convective heat transfer inside the honeycomb channels shows a resonant behavior at low frequencies and is responsible for

the increase in heat release rate from the flame. This argument goes against the hypothesis proposed by Khanna [1] which theorizes that convection does not play any role in the creation of the heat transfer resonance in the flat flame burner. The temporally varying heat source case has shown that the low frequency resonance occurring in the flat flame burner is due to the heat transfer coupling between the flame and the honeycomb and is not related to chemical dynamics. Perhaps, this is the reason why the current work which incorporates two-step curve fit chemistry modeling is able to predict the low frequency resonance phenomenon as well as the 1-D study conducted by Haber [84] that included detailed CH_4-air chemistry modeling.

6.5 Fuel Variability Study: Propane-air Mixture

The analysis of the laminar flame dynamics by CFD modeling using premixed methane-air showed that the flame speed oscillations define the dynamic behavior of the flame. Heat transfer was found to be responsible for the $30\,Hz$ resonance phenomena captured by the single channel CFD model. It is expected that by changing the fuel (hence changing the mean heat release rate), the resonant phenomena should not move to another frequency. This is because the heat transfer characteristics of the system remain unchanged with a change of the fuel. To confirm this hypothesis, the fuel was changed to propane and a single channel simulation was performed. The modeling parameters remained the same for this study except for the chemistry mechanism – a two step chemistry mechanism for propane-air combustion was chosen from FLUENT's chemical database. The flat flame in the simulation was perturbed by incoming velocity oscillations and an FRF between unsteady velocity and unsteady heat release rate was obtained. The FRF is shown in Figure 6.21. As expected, the low frequency pulsating instability was captured at $30\,Hz$ by the CFD model. Therefore, it can be conclusively said that the heat transfer coupling between the flame (oscillating heat source) and the honeycomb heat transfer to the incoming fuel-air mixture (oscillating velocity) is responsible for the $30\,Hz$ pulsating instability.

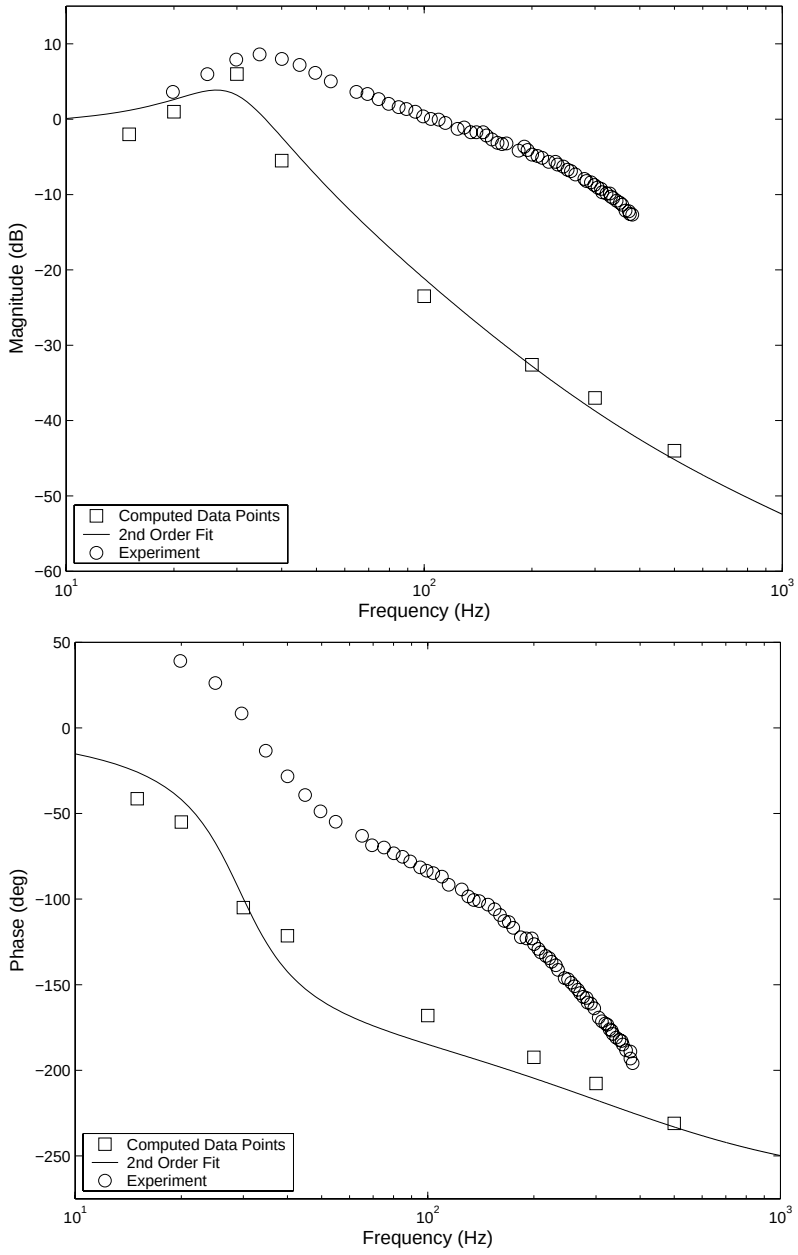

Figure 6.21: Single channel frequency response function magnitude and phase (Propane-air mixture, $Q = 200\,cc/s$ and $\phi = 0.75$)

Figure 6.22 shows the comparison between methane-air combustion FRF and propane-air combustion FRF. The rolloff at higher frequencies is less for the propane-air flame ($35\,dB$ per decade) as compared to the methane-air flame ($45\,dB$ per decade). The gain at $30\,Hz$ (the resonance frequency for both methane-air combustion and propane-air combustion) is higher for the propane-air case. The higher gain exhibited by propane-air FRF implies that for the same equivalence ratio, propane-air flames will tend to get unstable for less gain as compared to methane-air flames. Experimental studies [1] have also shown that premixed propane air flames are more susceptible to thermoacoustic instabilities as compared to methane-air flames. For the propane-air case, the phase predicted between unsteady heat release rate and incoming mass-flux oscillations is similar to the methane-air case. Both cases show a phase drop of approximately 240° between $0\,Hz$ and $500\,Hz$. The phase captured in the experimental study also shows that there is no effect of choice of fuel on the phase drop.

6.6 Summary

In this part of the study, laminar flat flames stabilized on a honeycomb burner were perturbed by incoming mass-flux oscillations. A FRF was generated between the unsteady heat release rate (q', output) and the incoming velocity oscillations (u', input). The following points summarize the results obtained for the laminar flat flame part of the study:

1. For methane-air flames, the FRF obtained from a single channel simulations of the flat flame showed better match with experimentally obtained FRF compared to the result of the full 2-D study. The low frequency resonance observed in experiments (at $32.5\,Hz$) was captured by the CFD model (predicted frequency of $30\,Hz$). The phase between q' and u' showed a drop of 180° between $15\,Hz$ and $75\,Hz$, indicating that the system was lightly damped.

2. A non-reacting flow heat transfer study conducted on the same flow configuration and geometry showed that the low frequency resonance phenomenon (at $30\,Hz$) occurs

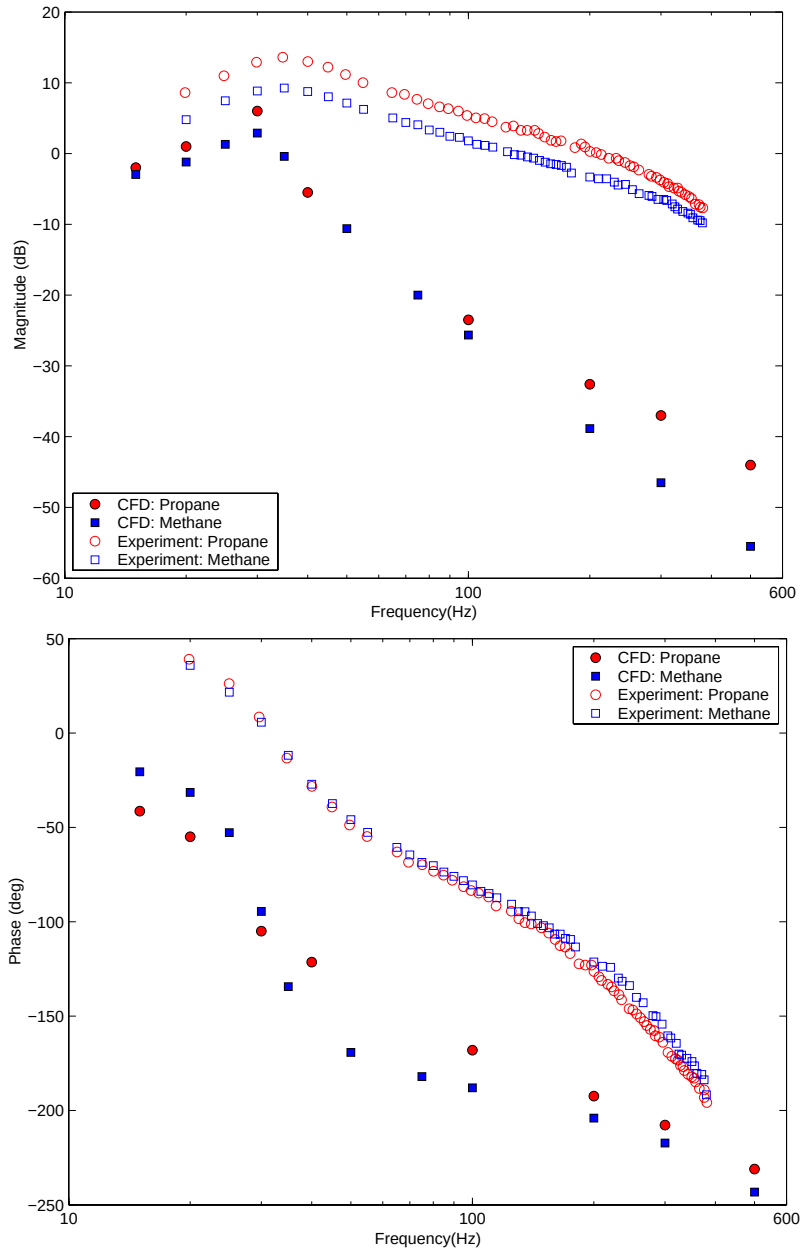

Figure 6.22: Comparison of frequency response function magnitude and phase between methane-air combustion and propane-air combustion ($Q = 200\,cc/s$ and $\phi = 0.75$). The CFD data from the two single channel simulations are shown by solid symbols.

because of the presence of two elements – the oscillating mass-flux and the oscillating heat release rate from the flame (in the heat transfer study, the flame is replaced by a heat source oscillating in time). For a resonance to occur, a second order system (with two forcing functions) must be present. In the study, it was also shown that the two sources need to be out of phase to create the low frequency resonance.

3. The effect of fuel variability using a propane-air mixture was conducted to compare the effect of two different fuels on the FRF. It was observed that the propane-air flame exhibited very similar dynamic characteristics as the methane-air flame. The gain for all frequencies was higher for the propane-air flame, showing that the propane-air flame will be more susceptible to thermoacoustic instabilities. The phase predicted for the propane-air flame was observed to follow the methane-air flame phase closely.

Further investigation of the effect of velocity perturbations on flame heat release rate was explored and is presented in the turbulent flame dynamics part of the study which follows. Since all gas turbine combustors involve a turbulent combustion regime, it is important to investigate the effect of the 'noisy' flow on the flame transfer function.